JOURNAL OF PROPULSION AND POWER
Vol. 24, No. 4, July–August 2008

Flame Characteristics in Supersonic Combustor with Hydrogen Injection Upstream of Cavity Flameholder

Ming-Bo Sun,* Zhen-Guo Wang,† Jian-Han Liang,‡ and Hui Geng§
National University of Defense Technology, 410073 Changsha, People's Republic of China

DOI: 10.2514/1.34970

Flame characteristics and a plausible flameholding mechanism in a supersonic combustor, with hydrogen injection upstream of a cavity flameholder, were investigated in the present study. Instantaneous OH radical distribution of the combustion flowfield was obtained using OH planar laser-induced fluorescence. According to the similarity of experimental observations with different cavities, a typical $L/D = 7$ cavity was chosen, and its supersonic combustion flowfield with hydrogen injection was calculated by large-eddy simulation. The results showed that the cavity shear layer plays a very important role in the flameholding process. An approximately steady flame existed in the cavity shear layer and hot combustion products were transported into the injection jet by the vortex interaction of the jet-with-cavity shear layer. Flame then spread gradually following the counter-rotating vortex induced by the jet until the whole injection jet was ignited. Combustion products, which generated from the cavity shear layer and the jet, were convected into the cavity by the unsteady motion of the cavity shear layer and transported with the recirculation flow to the cavity front wall. These hot products and their intermittent combustion then heated up the cavity, and the fuel that entered into the cavity shear layer was preheated. Thus, the flameholding cycle was formed.

I. Introduction

SCRAMJET engines are promising candidates for future airbreathing propulsion systems. At flight speeds beyond Mach 6, air entering the combustor must be supersonic to avoid excessive dissociation of both nitrogen and oxygen gases. Because of the inherent difficulties associated with combustion in a supersonic flow (i.e., slow overall kinetic rates and very short combustor residence times), the need exists for development of robust flameholding schemes for practical use. One candidate for such a flameholder is the wall cavity. Wall cavities are typically characterized as either open or closed. For scramjet applications where drag is a key consideration [1], open cavities are desirable because they impose a smaller drag penalty on the engine. Open cavities exposed to a flow experience self-sustained oscillations, which may induce intense fluctuating pressures, densities, and velocities in and around the cavity. To guarantee a stable combustion process, cavity flameholders with slanted rear walls are commonly used. For robust flameholding techniques, comprehensive understanding of flame stability in cavities has become a research issue of practical and scientific importance.

Among the various injection schemes, transverse fuel injection into a combustor appears to be the simplest and has been used in several engine programs, such as the Hyshot Scramjet engine.[¶] Ben-Yakar [2] observed the unstable injection jet in their supersonic combustion experiment with Mach 3.71. They also studied the interaction between the jet and cavities based on the side-view OH planar laser-induced fluorescence (PLIF) and schlieren images. Gruber et al. [1] studied the mixing and combustion characteristics of cavities in supersonic flow using NO-PLIF and OH-PLIF. Li et al. [3] obtained the side view of OH distribution of an H2 jet upstream of the cavity in Mach 2.0 freestream, but did not obtain OH distributions in other directions. Transverse injection into a supersonic crossflow and its interaction with cavity flameholders exhibit high unsteadiness, which are of significant interest in topics at present due to their influence on supersonic combustion procedure. Ben-Yakar [2] showed that supersonic combustion is overlaid with the large-eddy motions of the unstable injection jet. Choi et al. [4] presented detached-eddy simulation (DES) combustion computations for a two-dimensional scramjet combustor configuration with transverse fuel injection and a cavity flameholder. Choi et al. [4] demonstrated the injector flow instability and the cavity-driven instabilities, but the absence of experimental tests and the two-dimensional calculation make the results incomplete. Genin and Menon [5] conducted a three-dimensional large-eddy simulation (LES) calculation to study hydrocarbon liquid fuel spray combustion upstream of a cavity, but his result is relatively coarse and there was no comparison with experimental data. Li et al. [6] established an integrated theoretical/numerical framework to investigate the combustion oscillations in a scramjet combustor equipped with a cavity flameholder from the experiments of Ma et al. [7].

Traditional flameholding models may be not appropriate for cavities because the short combustor residence time invalidates the common assumption that reactants are premixed entering the combustion region. Recirculation in the cavity also adds new complexities to modeling efforts. Davis and Bowersox established the mathematic model [8] using perfect stirred reactor analysis and estimated the initial cavity size based on the lower residence time (defined as the residence time required to sustain combustion) of the cavity. However, the analytical model met problems on the residence time calculations because some of the calculated results were contradictory when different turbulent models were used [9]. Blowout limits, flame chemiluminescence, and nonreacting mixing patterns have been quantified in previous reports [1,10,11]. Despite these efforts, the physical mechanism of flameholding is not well understood. Designers will require more detailed physical understanding of where the reactions take place and the impact of the jet and cavity on the combustion process. From a scientific standpoint, new research efforts are warranted to extend the knowledge of flameholding phenomena to include nonpremixed conditions and cavity configurations. Ben-Yakar [2] made an elementary discussion about the ignition and flameholding mechanism around cavities based on their OH-PLIF experiments.

Received 5 October 2007; accepted for publication 17 March 2008.

*Ph.D. Candidate, Department of Aerospace Science and Technology, College of Aerospace and Material Engineering; wind_flowcfd@163.com.

†Professor, Department of Aerospace Science and Technology, College of Aerospace and Material Engineering; Zhenguo_Wang@nudt.edu.cn.

‡Professor, Department of Aerospace Science and Technology, College of Aerospace and Material Engineering; jhleon@vip.sina.com.

§Ph.D. Candidate, Department of Aerospace Science and Technology, College of Aerospace and Material Engineering; genghui@163.com.

¶Hyshot projects, http://www.uq.edu.au/hypersonics.2008.

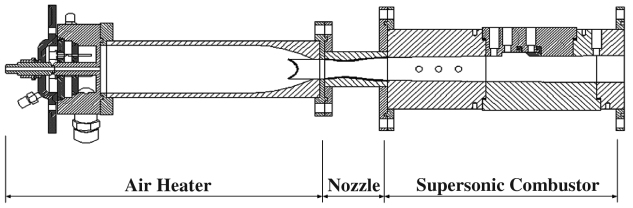

Fig. 1 Schematic of experimental facility.

Rasmussen et al. [12] discussed the flameholding mechanism of the combustor with directly injecting hydrocarbon fuel into the cavity flameholder using OH-PLIF and CH_2O-PLIF.

In the present study, the characteristics of supersonic combustion of hydrogen injected upstream of a cavity-based flameholder in a scramjet combustor is investigated using OH-PLIF and LES. The flame characteristics and its plausible stabilization mechanism will be discussed. This work is part of an ongoing research program aimed at providing information to help improve the overall understanding of cavities for use as scramjet flameholders.

II. Experimental Descriptions

The experimental facility can be seen in Fig. 1. The model scramjet combustor is directly installed behind the nozzle of the air heater, which heats the air by means of air/O_2/H_2 combustion. Flow conditions at the nozzle exit are listed in Table 1 and the O_2 mass fraction is 23.3% in the vitiated air to simulate the real air stream. The jet conditions in the experiments are shown in Table 2.

The cross-sectional area is 32.6×44 mm at the exit of the facility nozzle. The combustor has a constant width of 44 mm, and an expand angle of 1 deg on the top wall side. The cavity and the injector are mounted on the bottom side. The length of the combustor is 400 mm.

The cavity used is set as $L/D = 4$ or $L/D = 7$, and every configuration has two depths ($D = 5$ mm and $D = 8$ mm). The cavity is built when different model configurations are inserted on a cavity base (shown in Fig. 2). All cavities have an aft wall angle of 45 deg. An injector (orifice exit diameter = 2 mm) is installed 127 mm downstream of the nozzle exit. The distance from the injector centerline to the cavity front wall is 10 mm.

Three quartz glass windows are mounted on the combustor to allow optical access. The PLIF system includes an Nd:YAG laser, a dye laser, a frequency doubler, and an intensified charge-coupled device (ICCD) system, as shown in Fig. 3. The output beam from the Nd:YAG laser is at 532 nm. It pumps the dye laser to generate the laser beam at 567.106 nm. Then the output from the dye laser is transferred into the doubler, which transforms it into a UV laser beam at 283.553 nm. This wavelength is located at the transition Q1(8) of the OH radical. The UV beam is adjusted to a laser sheet by a group of lenses. The thickness of the plane beam is about 0.2 mm and the width is about 32 mm. The PLIF image is photographed by an ICCD camera. Two sets of filters are mounted in front of the camera. The filter set is made up of UG11 and WB305, as shown in Fig. 3. The exposure time of PLIF is 100 ns.

III. Theoretical Formulation and Numerical Treatment

A. Governing Equations

The flowfield is three-dimensional and can be described with the conservation equations for a multicomponent chemically reactive system. The filtered coupled form of the species conservation, fluid dynamics, can be summarized in a conservative vector form as follows:

$$\frac{\partial \bar{\rho}}{\partial t} + \frac{\partial(\bar{\rho}\tilde{u}_i)}{\partial x_i} = 0 \tag{1}$$

$$\frac{\partial(\bar{\rho}\tilde{u}_i)}{\partial t} + \frac{\partial[\bar{\rho}\tilde{u}_i\tilde{u}_j + \bar{p}\delta_{ij} - \bar{\tau}_{ij} + \tau_{ij}^{\mathrm{sgs}}]}{\partial x_j} = 0 \tag{2}$$

$$\frac{\partial \bar{\rho}\tilde{E}}{\partial t} + \frac{\partial[(\bar{\rho}\tilde{E} + \bar{p})\tilde{u}_i + \bar{q}_i - \tilde{u}_j\bar{\tau}_{ji} + H_i^{\mathrm{sgs}} + \sigma_i^{\mathrm{sgs}}]}{\partial x_i} = 0 \tag{3}$$

$$\frac{\partial \bar{\rho}\tilde{Y}_k}{\partial t} + \frac{\partial}{\partial x_i}\left(\bar{\rho}\tilde{Y}_k\tilde{u}_i - \bar{\rho}\tilde{Y}_k\tilde{V}_{i,k} + Y_{i,k}^{\mathrm{sgs}} + \theta_{i,k}^{\mathrm{sgs}}\right) = \bar{\dot{\omega}}_k \tag{4}$$

where $\bar{q}_i$ is the heat flux vector,

$$\bar{q}_i = -\bar{\kappa}\frac{\partial \tilde{T}}{\partial x_i} + \bar{\rho}\sum_{k=1}^{N}\tilde{h}_k\tilde{Y}_k\tilde{V}_{i,k} + \sum_{k=1}^{N} q_{i,k}^{\mathrm{sgs}}$$

The diffusion velocities are approximated using Fickian diffusion as

$$\tilde{V}_{i,m} = -\frac{\bar{D}_m}{\tilde{Y}_m}\frac{\partial \tilde{Y}_m}{\partial x_i}$$

The total subgrid stress tensor (SGS) is τ_{ij}^{sgs}, which can be expressed as

$$\tau_{ij}^{\mathrm{sgs}} = -2\overline{\rho}\nu_t[\tilde{S}_{ij} - \frac{1}{3}\tilde{S}_{kk}\delta_{ij}] + \frac{2}{3}\overline{\rho}k^{\mathrm{sgs}}\delta_{ij}$$

Therefore, to complete the closure for the subgrid stresses, the subgrid eddy viscosity ν_t and the subgrid kinetic energy k^{sgs} need to be modeled. The SGS model will be given in Sec. III.B.

$H_i^{\mathrm{sgs}}, \sigma_{ij}^{\mathrm{sgs}}, Y_{i,k}^{\mathrm{sgs}}, q_{i,k}^{\mathrm{sgs}}, \theta_{i,k}^{\mathrm{sgs}}$ are subgrid enthalpy flux, subgrid viscous work, convective species flux, subgrid heat flux, and subgrid species diffusive flux, respectively. The modeling for them can be shown as

$$H_i^{\mathrm{sgs}} = \frac{-\bar{\rho}\nu_t}{\mathrm{Pr}_t}\frac{\partial H_i}{\partial x_i}, \qquad Y_{i,k}^{\mathrm{sgs}} = \bar{\rho}\left[\widetilde{u_i Y_k} - \tilde{u}_i\tilde{Y}_k\right] = -\frac{\rho\nu_t^{\mathrm{sgs}}}{Sc_t}\frac{\partial \tilde{Y}_k}{\partial x_i}$$

and $\sigma_{ij}^{\mathrm{sgs}}, q_{i,k}^{\mathrm{sgs}}, \theta_{i,k}^{\mathrm{sgs}}$ can always be neglected.

The filtered reaction rate term is $\bar{\dot{\omega}}_k$ and its closure will be discussed in Sec. III.C.

Table 2 Injection conditions

	Jet
Stagnation temperature, K, T_0	300
Static temperature, K, T	250
Ratio of specific heats, γ	1.40
Stagnation pressure, MPa, P_0	0.7
Mach number, M	1.0
Injection port diameter, mm, d_{jet}	2.0

Table 1 Experimental conditions

Air heater		Nozzle exit				
Stagnation temperature, K	1221	Mach number	1.724			
Stagnation pressure, MPa	0.5	Static temperature, K	823			
Air mass flow rate, g/s	498.7	Static pressure, MPa	101			
O_2 mass flow rate, g/s	53.2	Mass fraction	O_2	H_2O	N_2	Others
H_2 mass flow rate, g/s	5.1		23.2%	8.1%	68.4%	0.3%

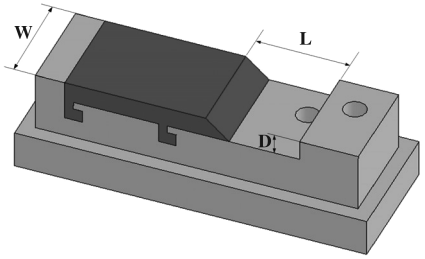

Fig. 2 Cavity setup and configuration.

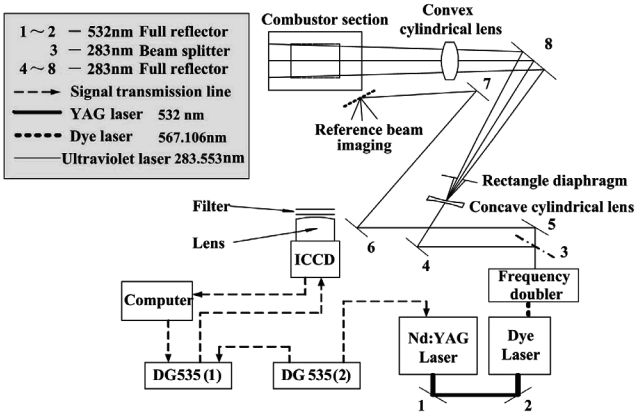

Fig. 3 OH-PLIF experimental setup.

B. Hybrid Reynolds-Averaged Navier–Stokes/Large-Eddy Simulation Methodology

Baurle et al. [13] had proposed a blending strategy referred to as hybrid (Reynolds-averaged Navier–Stokes) RANS/LES methodology. This method is believed to be more proper than the DES method initiated by Spalart et al. [14]. More comparisons about these two methods can be found elsewhere [13]. The hybrid formulation used in this paper is briefly given as follows.

Menter's k–ω baseline (BSL) model [15] is considered for the RANS portion:

$$\frac{\partial(\bar{\rho}\tilde{k})}{\partial t}+\frac{\partial(\bar{\rho}\tilde{k}\tilde{u}_j)}{\partial x_j}=\frac{\partial}{\partial x_j}\left[\left(\mu_l+\frac{\mu_t^{\mathrm{RANS}}}{\sigma_{k_1}}\right)\frac{\partial\tilde{k}}{\partial x_j}\right]+P_k-C_{d_1}\bar{\rho}\tilde{k}\tilde{\omega} \tag{5}$$

The SGS model chosen is the one-equation model used by Yoshizawa and Horiuti [16]:

$$\frac{\partial(\bar{\rho}\tilde{k})}{\partial t}+\frac{\partial(\bar{\rho}\tilde{k}\tilde{u}_j)}{\partial x_j}=\frac{\partial}{\partial x_j}\left[\left(\mu_l+\frac{\mu_t^{\mathrm{sgs}}}{\sigma_{k_2}}\right)\frac{\partial\tilde{k}}{\partial x_j}\right]+P_k-C_{d_2}\bar{\rho}\frac{\tilde{k}^{\frac{3}{2}}}{\Delta} \tag{6}$$

Multiplying the RANS eddy viscosity and the TKE (turbulent kinetic energy) equation by a blending function F, and the SGS viscosity and TKE equation by $(1-F)$ yields the desired hybrid model equation:

$$\begin{aligned}\frac{\partial(\bar{\rho}\tilde{k})}{\partial t}+\frac{\partial(\bar{\rho}\tilde{k}\tilde{u}_j)}{\partial x_j}&=\frac{\partial}{\partial x_j}\left[\left(\mu_l+\frac{\mu_t}{\sigma_k}\right)\frac{\partial\tilde{k}}{\partial x_j}\right]\\&+P_k-\bar{\rho}\left[FC_{d_1}\tilde{k}\tilde{\omega}+(1-F)C_{d_2}\frac{\tilde{k}^{\frac{3}{2}}}{\Delta}\right]\end{aligned} \tag{7}$$

where

$$\mu_t=\bar{\rho}[F\mu_t^{\mathrm{RANS}}+(1-F)\mu_t^{\mathrm{sgs}}],\qquad \frac{1}{\sigma_k}=\frac{F}{\sigma_{k_1}}+\frac{1-F}{\sigma_{k_2}}$$

The constant model values are σ_k, σ_{k_1}, and σ_{k_2} (see [13]). The distance-dependent blending function F has no universal formulation and several formulations have been given. Fan et al. [17] modified the blending function presented by Menter (see [15]) and used it for hybrid RANS/LES in the same framework. Baurle et al. [13] redefined the blending function using ideas borrowed from limited numerical scales hybrid approach to prohibit LES on coarse grids. Xiao et al. [18] gave a different formulation according to the ratio of RANS turbulence length scale to LES scale. But the present blending function has common problems that hybrid models always overpredict the separation region when solving adverse-pressure gradient flows (jet, shock/boundary-layer interaction, etc). Though the recycling method developed in recent years can improve the prediction [18], it is less effective to be implemented in complex flows. Therefore, an effective way is to improve the blending function to change the shift position of RANS and LES.

A baseline blending function formulation from Fan et al. [17] is given next:

$$F=\tanh(\eta^4)\quad\text{and}\quad\eta=\max\left(\frac{\sqrt{\tilde{k}}}{0.09\omega d},\frac{500\nu}{\omega d^2}\right)$$

where d is the distance to the nearest wall.

This baseline hybrid model will overpredict the separation region of the adverse-pressure gradient flow. To solve this problem, Menter [15] defined another blending function to avoid the overprediction of separation.

$$F_2=\tanh(\eta^2)\quad\text{and}\quad\eta=\max\left(2\cdot\frac{\sqrt{\tilde{k}}}{0.09\omega d},\frac{500\nu}{\omega d^2}\right)$$

The function is one for boundary-layer flows and zero for free shear layers. Our tests showed that this is an overcautious blending function because it contaminates the whole boundary layer by using RANS, and even affects some regions above the boundary layer. An improved blending function is defined as

$$F_{\mathrm{new}}=\tanh(\eta^4)\quad\text{and}\quad\eta=\max\left(\alpha\cdot\frac{\sqrt{\tilde{k}}}{0.09\omega d},\frac{500\nu}{\omega d^2}\right)$$

where α is a constant which needs determination and we believe $\alpha=1.505$ is a proper choice based on the validation [19].

C. Chemical Reactions

The mechanism for hydrogen–air combustion consists of six reactive species (H, H_2, O, O_2, H_2O, OH) and eight reaction steps. Nitrogen is assumed as an inert gas because the oxidation process does not have a significant affect on the fluid dynamics in a combustor.

The elementary reaction steps are generally expressed as

$$\sum_{k=1}^{N}\nu'_{k,r}X_k\leftrightarrow\sum_{k=1}^{N}\nu''_{k,r}X_k$$

The mass production rate of each species is written as

$$w_k=M_k\sum_{r=1}^{Nr}(\nu''_{k,r}-\nu'_{k,r})\left[k_{\mathrm{fr}}\prod_{k=1}^{N}\left(\frac{\rho Y_k}{M_k}\right)^{\nu'_{k,r}}-k_{\mathrm{br}}\prod_{k=1}^{N}\left(\frac{\rho Y_k}{M_k}\right)^{\nu''_{k,r}}\right]$$

where $k_{\mathrm{fr}}=A_rT^{B_r}e^{-E_r^*/RT}$

The reaction coefficients in the formula k_{fr}, k_{br} are taken from [20].

The closure problem for the interaction of turbulence and chemistry is an important issue in supersonic combustions. Recently, there were many attempts to address this issue using probability density functions, linear eddy model approaches, and other combustion models extended from subsonic combustion conditions. Although useful advances were achieved, the improvement was insignificant in comparison with the results from laminar chemistry and existing experimental data, as evidenced in the results by Möbus et al. [21]. By examining the existing results, such as Norris and Edwards [22], it is thought that the solution accuracy seems to be more dependent on grid resolution than the modeling of turbulence–chemistry interaction.

In view of the lack of reliable models for turbulence–chemistry interactions, especially for supersonic flows, the effect of turbulence on chemical reaction rate is ignored in the present work. However, a hybrid RANS/LES approach with a massive computational grid is used for the highly refined combustion characteristics overlaid with large-eddy motions of unstable injector flow.

D. Numerical Scheme and Boundary Condition Specification

The equation set describing chemically reacting flows is difficult to solve because it is mathematically stiff. Stiffness can be defined as the ratio of the largest to the smallest time scale. In reacting flows, the time scales associated with the chemistry tend to be much smaller than the time scale of fluid motion, sometimes by orders of magnitude. There are currently two approaches to solving stiff systems of equations. One approach is to uncouple the fluid dynamics equations from the rate equations. Each time step consists of a fluid dynamics step with frozen chemistry, followed by a chemical reaction step (or several small steps) without flow interaction. The second approach solves the fully coupled equation set simultaneously. This approach requires an implicit treatment of the chemical source terms that essentially rescales the equations in time so that all events occur on a similar pseudotime scale. The obvious deficiency of this approach is the high cost of calculating the matrix for full or point-implicit implementation. In this paper, the uncoupled solver is chosen and its efficiency has been validated [23].

Studies of errors in LES have demonstrated that numerical schemes must be chosen with care. Studies of Blin et al. [24] showed that second-order accurate schemes and a third-order WENO (weighed essentially nonoscillation) scheme clearly underestimate the turbulent kinetic energy. The large scales of the flow suffer from the high numerical dissipation, whereas results of a fifth-order WENO scheme agrees well with the direct numerical simulation data. Based on this, a fifth-order WENO scheme is used here for inviscid fluxes. The time integration is performed by means of a two-order accurate total-variation-diminishing Runge–Kutta method proposed by Shu [25]. The Courant-Friedrichs-Lewy number is fixed to 0.5. The splitting of convective species flux is uncoupled from the Navier–Stokes equations and based on the splitting result of the convective density flux. Simplified point-implicit formulation is adopted to deal with the stiffness generated by the chemical reacting source term of every separate species equation.

A no-slip, no-penetration adiabatic condition is imposed at all walls and a zero-gradient condition is enforced at the outflow boundary. Supersonic inflow boundary conditions are enforced just upstream of the cavity leading edge. For the fifth-order WENO scheme, three extra points (called ghost points) are needed for the requirements of the spatial derivatives near boundaries. To enforce the physical boundary conditions, numerical boundary conditions have to be applied to these ghost points. For a solid boundary, the reflective boundary condition is employed. For the inflow/outflow boundary, the nonreflective boundary condition is implemented.

IV. Results

A. OH-PLIF of the Reacting Flowfields

For streamwise view (profile) images, the laser sheet is directed down through the top wall window and centered on the injection centerline; imaging occurs normal to the sheet through a side wall window. For spanwise (end) views, the sheet is transmitted over the test section span through the side wall windows, and imaging occurs from a side window. Because the camera is positioned at an off-normal angle to the sheet, the image is corrected for blur by employing a Scheimpflug mount. It is necessary to adjust the brightness scale on the resulting images to bring out features in the data that are not normally visible in the raw pictures. Marching the laser sheet downstream (x direction), the numbers shown in Figs. 4–7 represent the distance downstream of injection. Of interest is the discrepancy in the value of the local maximum in the mean OH images as the end view camera traverses downstream of the injection (positive x direction). The OH information is normalized by the value of reference beam images (seen in Fig. 3). For observation convenience, the PLIF images obtained are shown with reverse color.

The jet-without-flameholder experiments were tested at first but no combustion and flame were observed, which implied that flame cannot be stabilized without extra flameholders under such flow and jet condition. Figures 4–7 give the PLIF images of different cavities on the injection centerline and several spanwise locations, in which x' represents the distance between the injector centerline and the view location along the downstream direction, and the arrow represents the projected injection position in the spanwise plane. The images are obtained from different experiments and they have the same contour legend as shown in Fig. 4.

From Figs. 4–7, we can find that for cavities with different L/D and absolute depth, the OH radical distribution from the upstream injection reveals similar characteristics:

1) The PLIF signal near the injector is faint, which means the fuel jet does not ignite directly near the injector. The side views and the end views of OH radical demonstrate that the fuel jet starts to burn at some distance downstream of the cavity front wall, which indicates that the cavity played an important role in the fuel jet ignition and flame stabilization.

2) The OH-PLIF signal mainly exists in the cavity shear layer near the cavity front wall, which means that a portion of the fuel entrains into the cavity shear layer, mixes with air, and ignites ahead of the jet, above the cavity shear layer. The OH in the cavity shear layer is not entrained by the cavity recirculation zone because the signal intensity is stronger than that of the cavity bottom.

3) The OH radicals in the cavity shear layer are connected with OH radicals in the inclining fuel jet, which suggests significant interactions between the injection and the cavity shear layer.

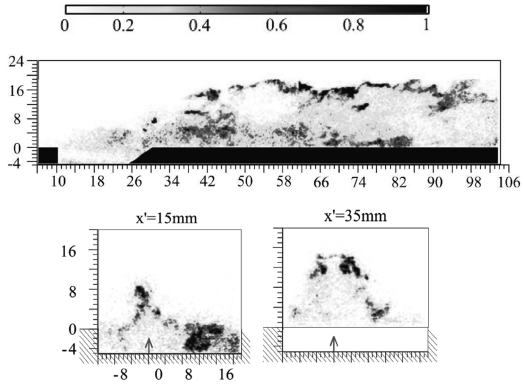

Fig. 4 OH-PLIF images of side view in centerline plane and end view in two axial locations downstream of the cavity $L/D = 4, D = 5$ mm.

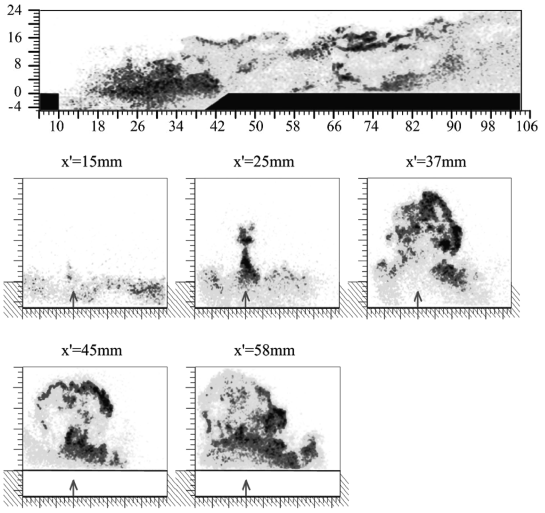

Fig. 5 OH-PLIF images of side view in centerline plane and end view in five axial locations downstream of the cavity $L/D = 7, D = 5$ mm.

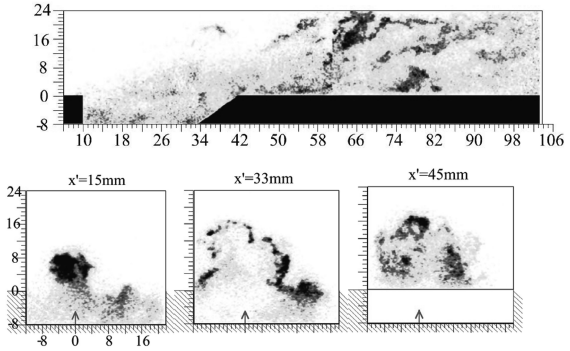

Fig. 6 OH-PLIF images of side view in centerline plane and end view in three axial locations downstream of the cavity $L/D = 4, D = 8$ mm.

OH radicals from the cavity shear layer, which can be identified, enter into the core of the jet near the cavity front wall. Then, the jet starts to burn entirely after a short streamwise distance. This phenomenon may result from the counter-rotating vortices induced by the jet, which absorb the products in the cavity shear layer into the core of jet, and further lift them up to the interface of the jet with the mainstream. The flame of the jet and the cavity shear layer penetrate into each other and the interface cannot be identified, especially in the region downstream of the cavity aft wall.

4) From side views of different cavities, we can see that the interface of the reacting jet in the streamwise plane is significantly distorted, which means large-scale structures might dominate the mixing process and affect the combustion. From end views of different cavities, we can also see that the interface of the reacting jet in the spanwise plane is highly distorted, which means the streamwise vortex structures affect the combustion process greatly.

5) Though discrepancies exist in the OH-PLIF image for different cavity reacting flowfields, the OH distributions are similar in streamwise and spanwise directions under the same jet condition.

The injection jet interaction with the cavity flow may dominate the fuel combustion, but the instantaneous PLIF images cannot give a time history of interaction (images are temporally uncorrelated). To reveal the cause of the OH distribution, the $L/D = 7$, $D = 8$ mm cavity is chosen and its flowfield is calculated with large-eddy simulation.

B. Instantaneous Combustor Flowfields by Large-Eddy Simulation

The length of the computational domain is 150 mm and the inlet of the domain is 34.1×22 mm. The computational section is cut from the test section, along the streamwise direction, 90 mm downstream of the nozzle exit. The top wall has an expand angle of 1 deg. The

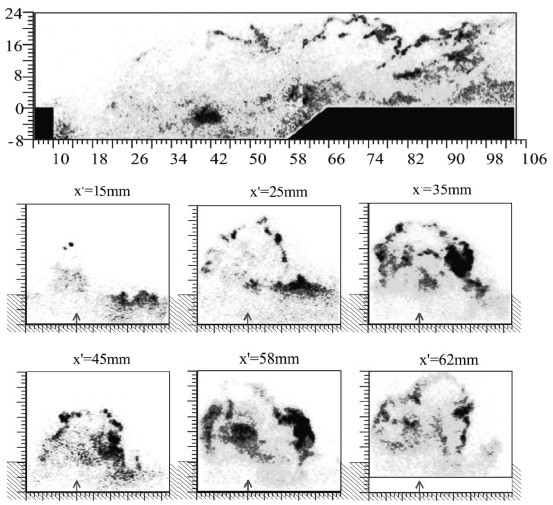

Fig. 7 OH-PLIF images of side view in centerline plane and end view in six axial locations downstream of the cavity $L/D = 7, D = 8$ mm.

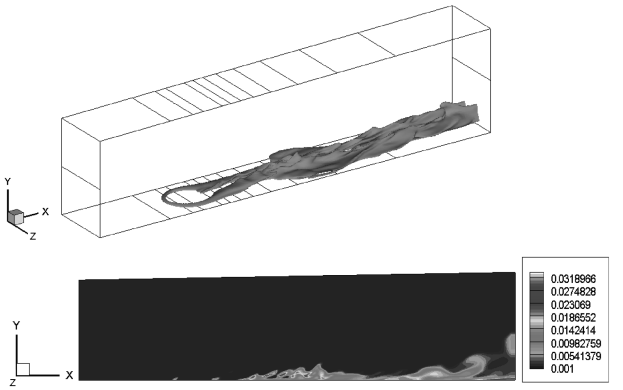

Fig. 8 Oblique view ($\tilde{y}_{OH} = 0.01$) and slice at $z = 11$ mm of instantaneous OH distribution.

numerical simulation reported here uses a $396 \times 121 \times 63$ grid in the streamwise, transverse, and spanwise directions and a $185 \times 41 \times 63$ grid in the cavity. The grid points were clustered near the jet orifice, the cavity front wall, and the aft wall in the streamwise and transverse direction. The jet orifice is resolved using 14×8 grid points. The thermophysical properties of the vitiated air and the hydrogen injection correspond to the parameters listed in Tables 1 and 2.

The current simulations are carried out on a distributed memory parallel processing computer (Intel Pentium, 3.0 GHz) using the message passing interface. Typically, 32 processors are employed and the whole grid is separated into 32 blocks for the cavity flowfield. For the jet-without-cavity case, 24 processors are employed.

1. *Jet-Without-Cavity Case*

For the jet-without-flameholder case, no combustion and flame were observed in the experiments under the jet and flow condition shown in Table 2. However, we calculate the jet-without-cavity combustion case to provide a reference flow for comparison with the jet-with-cavity case. Figures 8 and 9 show the instantaneous OH and H_2 distributions of the flowfields at the time moment $t = 80t_c$ ($t_c = D/U_\infty$). The so-called horseshoe vortex (HSV), which is

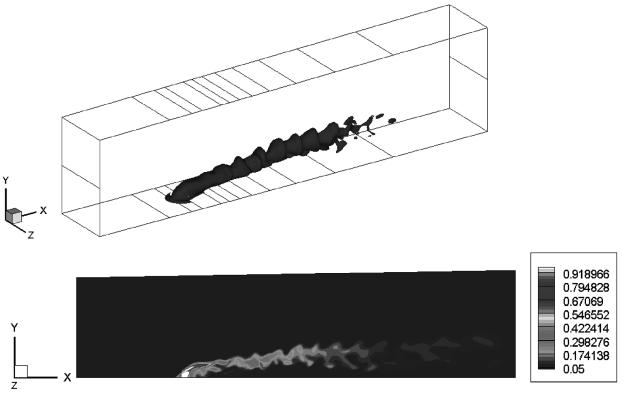

Fig. 9 Oblique view ($\tilde{y}_{H_2} = 0.01$), and slice at $z = 11$ mm of instantaneous H_2 distribution.

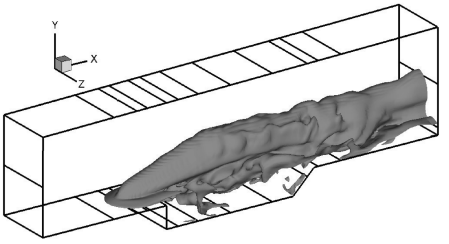

Fig. 10 Oblique surface view ($\tilde{y}_{H_2} = 0.0015$) of instantaneous H_2 distribution.

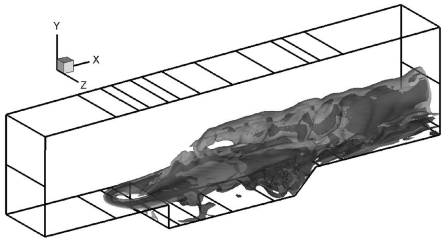

Fig. 11 Oblique surface view ($\tilde{y}_{OH} = 0.0015$ and $\tilde{y}_{OH} = 0.015$) of instantaneous OH distribution; dark gray signifies higher concentration.

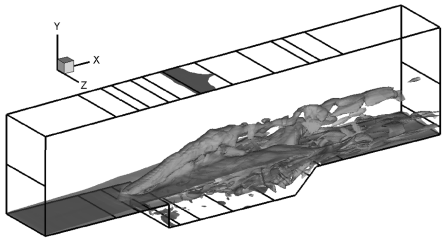

Fig. 12 Oblique view, instantaneous isosurface of spanwise vortex structure ($\omega_z = 0.5$).

marked with chemical radicals, can be seen in Fig. 8. It has an omega-shaped structure that wraps the jet column and stays fairly close to the plate surface. The injection has not been ignited and the reacting region is mainly distributed in the boundary layer. After a long distance downstream of the injector, nearly at the exit of the computational domain, the bottom of the jet begins to burn. From the figures, the separation region near the jet plays an important role in ignition. However, it should be pointed out that the ignition cannot be stabilized in experiments because the separation region around the jet is highly unsteady, which might be the reason why no combustion and flame were observed under the jet condition shown in Table 2.

2. Supersonic Combustion of Hydrogen Injection Upstream of a Cavity Flameholder

Figures 10 and 11 show the instantaneous OH and H_2 distributions of the flowfield at the time moment $t = 80t_c$ ($t_c = D/U_\infty$). In comparing these figures with the distribution in the jet-without-cavity case, the jet has been ignited after a short distance downstream of the cavity front wall. This is caused by the unsteady distorted cavity shear layer. Figures 12 and 13 reveal the vortex structures of the

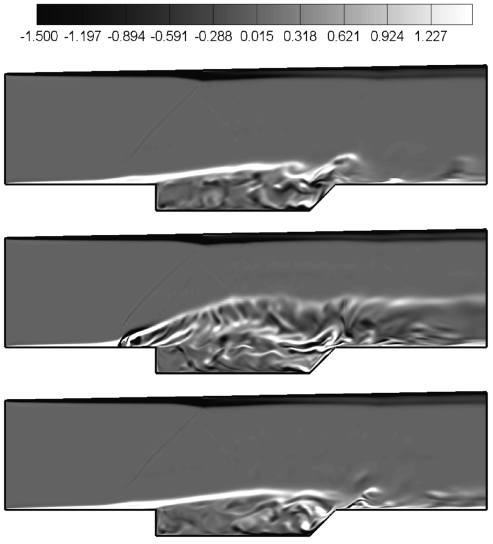

Fig. 13 Slice at $z = 5$, 11, and 17 mm, respectively; instantaneous contours of spanwise vortex structure.

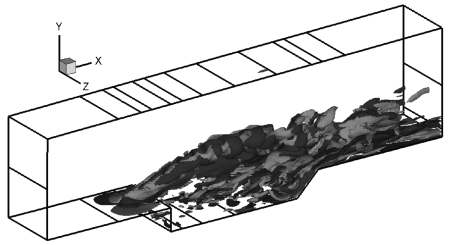

Fig. 14 Oblique view, instantaneous isosurface of streamwise vortex structure ($\omega_x = -0.5$ and $\omega_x = 0.5$).

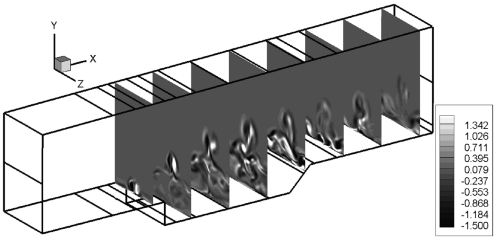

Fig. 15 Oblique view of axial slices at $x = 132.5$, 147.0, 168, 162.0, 176.0, 191, 205, 220, and 235 mm; instantaneous contours of steamwise vortex structures.

flowfield at the time moment $t = 80t_c$. Figure 12 shows the spanwise vortex structures of the instantaneous flowfield, from which we can see that large-scale shear layer vortices emanate at the jet/freestream interface. The initial growth of the cavity shear layer is dominated by elongated Kelvin–Helmholtz structures. At a distance away from the cavity front wall, these structures break down in a highly three-dimensional fashion. However, the cavity shear layer under the declining jet demonstrates high instabilities as soon as it is shed from the cavity front wall, and numerous spanwise vortices originate and convect downstream. This phenomenon can be seen more clearly in the slices shown in Fig. 13. In the centerline plane (where $z = 11$ mm), the injection jet upstream induces small vortices in the frontal shear layer and makes the shear layer motion different from the slices of $z = 5$ mm and $z = 17$ mm. The interaction of the cavity shear layer with the jet will promote the mass exchange between the cavity and the main stream, which is propitious to hold flame. Figure 14 shows the streamwise vortex structures of the flowfield. The HSV, closest to the jet injection, has an omega-shaped structure

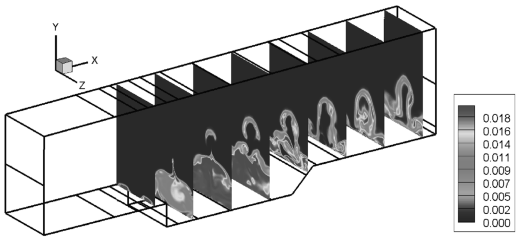

Fig. 16 Oblique view of axial slices (for slice position, see Fig. 15); instantaneous contours of steamwise OH distribution.

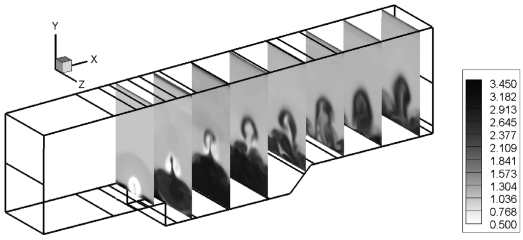

Fig. 17 Oblique view of axial slices (for slice position, see Fig. 15); instantaneous contours of steamwise temperature distribution.

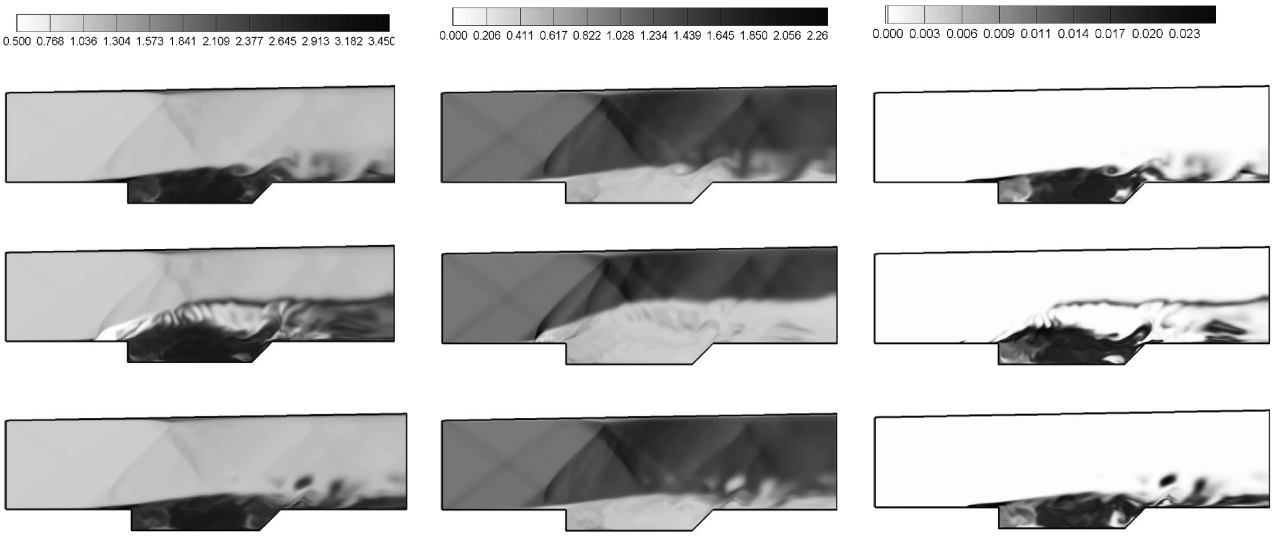

a) Temperature distribution **b) Density distribution** **c) OH radical distribution**

Fig. 18 Slices at $z = 5, 11, 17$ mm; instantaneous contours of a) temperature distribution, b) density distribution, and c) OH radical distribution.

that wraps the jet column and stays fairly close to the plate surface. The counter-rotating structures can also be seen in Fig. 14, but more clearly in the contour slices of Fig. 15. The pair of counter-rotating vortices induce each other and gradually lift along the streamwise direction. The streamwise vortices in the cavity shear layer develop very quickly, especially under the declining jet. The intensity of the streamwise vortices in the shear layer near the cavity aft wall is of the same order with the spanwise vortices.

Comparing Figs. 10 and 14, we can clearly see that a portion of the hydrogen fuel enters into the cavity shear layer, following the horseshoe vortex and the vortex interaction of jet-with-cavity shear layer. The coherent structures have entrained the high-temperature reactive products from the cavity into the cavity shear layer, so that a portion of the fuel is mixed with the high-temperature gaseous products and ignited some distance after injection. This explains the reason why a continuous flame exists in the cavity shear layer from Figs. 10–15.

Effects of the counter-rotating structures on the combustion process can be seen clearly in the contour slices of Figs. 16 and 17. The pair of the counter-rotating vortices absorb the high-temperature products in the cavity shear layer. The OH radicals and high-temperature products follow the motion of the streamwise vortices, and the combustion region gradually diffuses into the core of the jet, which has also been observed in the OH-PLIF results. Then, flame spreads gradually, following with the counter-rotating vortex induced by the jet until the whole injection jet is ignited. The distributions of temperature, density, and OH radical are shown in Fig. 18. The density distribution (Fig. 18b) reveals that the oblique shock wave reflected from the upper wall impinges into the jet. Figure 18a shows that the temperature increase by the oblique shock wave is weak compared with the heat release of combustion before the shock wave. Figure 18c also shows that the OH radicals emerge before the shock wave impingement point, which means the jet has been ignited before the shock wave incidence.

C. Flame-Spreading and -Holding Mechanism of Injection Upstream of a Cavity Flameholder

A series of instantaneous flowfields of hydrogen combustion around the cavity flameholder are shown in Fig. 19. Compared with the jet-without-cavity case, the cavity shear layer provides highly unsteady exothermic flow with chemical radicals under the fuel jet. The instabilities evolving in the shear layer result in the unsteady periodic motion of the cavity shear layer, which may induce the pressure, temperature, and species fluctuation. Heat release might further excite the fluctuation. The large-scale vortices generated from the interaction of jet with the cavity shear layer can increase the interface of fuel and air and enhance the mass exchange process. In this regard, the high-temperature products in the cavity shear layer are likely to be taken into the core of the jet due to the unsteady fluctuation of the cavity shear layer. Then, it gets easier for the counter-rotating vortices to entrain the hot products and induce jet ignition, which might be the reason why the ignition position moves ahead and the delay distance of combustion is significantly shortened compared with the jet-without-cavity case. An indirect evidence from Fig. 19 is that the jet ignition position moves forward when the cavity shear layer deflects upward.

Figure 20 gives the schematic images to demonstrate the ignition process by the cavity shear layer. The figures illustrate that flame originates from the cavity shear layer, spreads with the counter-rotating vortex structures induced by the injection, and takes over the whole jet after some distance along the streamwise direction.

From Fig. 19, the flame in the cavity shear layer impinges with the aft wall and the jet flame curls into the cavity at the aft wall intermittently. Then, hot products are convected upstream through the recirculation zone and intermittent combustion occurs. This means that part of the combustion products generated from the cavity shear layer and the jet are convected into the cavity interior by the unsteady motion of the cavity shear layer, transported with the recirculation flow until it approaches the cavity front wall. These high-temperature products and the intermittent combustion heat up the whole cavity and help the cavity maintain a continuous environment with high temperature and plenty of reactive radicals. The cavity then preheats the fuel that enters into the cavity shear layer and, therefore, a flameholding cycle is formed.

Figure 21 gives the schematic images that demonstrate the flameholding process by the cavity. The figure demonstrates that the fuel jet is swept toward the cavity and is preheated as it moves toward the shear layer. Intermittent combustion occurs under the shear layer and throughout the area downstream of the cavity. Hot products are convected upstream through the recirculation zone where they are available to provide ignition energy to the incoming fuel. When a coupling of cavity shear layer unsteady motion and heat release is formed, the flame can be held. If heat release and the products transported into the cavity can increase the temperature to a high enough level, the ignition process of cavity shear layer and injection jet may occur and the flameholding cycle may be sustained.

V. Conclusions

In this paper, flame characteristics and a plausible flameholding mechanism in a supersonic combustor with hydrogen injection upstream of cavity flameholders are investigated using OH-PLIF

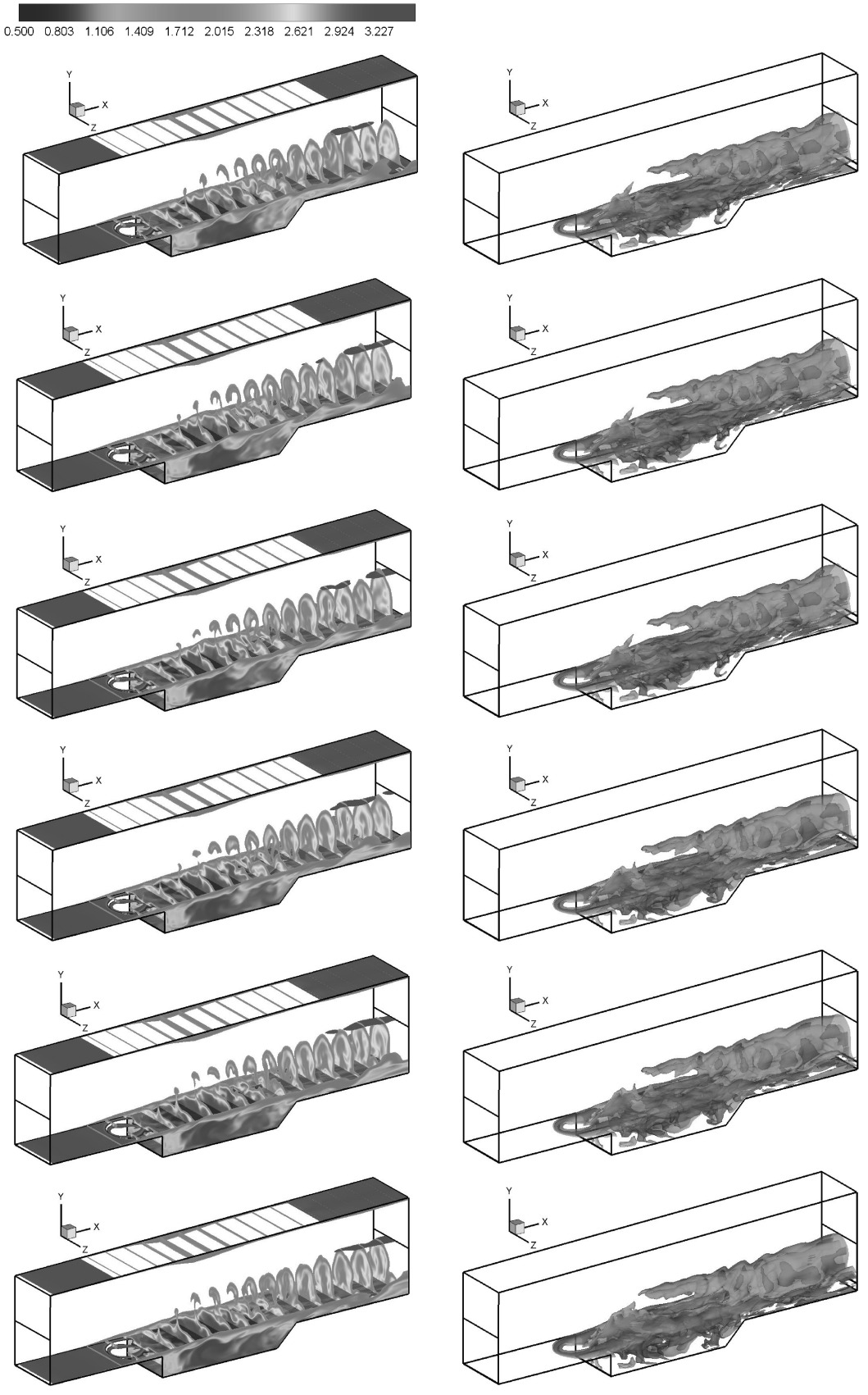

a) Temperature contours

b) OH radical isosurface views ($\tilde{y}_{OH}$=0.005 and $\tilde{y}_{OH}$=0.018)

Fig. 19 End views of axial slices; instantaneous contours of OH radical distribution at six different times with consistent time step ($\Delta t = 1.2t_c$, $t_c = D/U_\infty$).

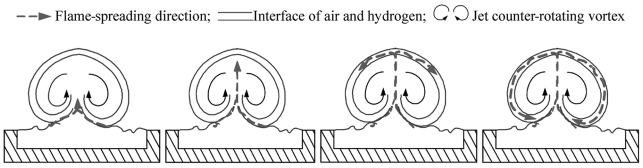

Fig. 20 Schematic of flame-spreading around the jet due to the counter-rotating vortex.

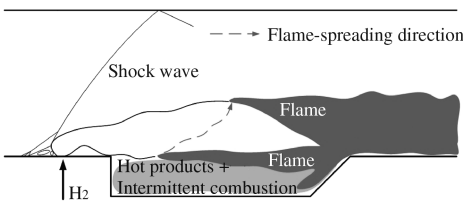

Fig. 21 Schematic of stabilization mechanisms as inferred from PLIF images and calculations. Flame is shaded dark gray. Light gray signifies hot products and convecting OH, unless otherwise marked.

and large-eddy simulations. Instantaneous OH radical distribution of the combustion flowfield in the streamwise and spanwise directions are obtained using OH-PLIF. According to the similarity of experimental observations with different cavities, a typical $L/D = 7$ cavity with an aft wall angle of 45 deg is chosen, and its supersonic combustion flowfield with hydrogen injection is calculated by large-eddy simulation. The calculated data and the experimental images both show that the cavity shear layer plays a very important role in the flameholding process. An approximately steady flame exists in the cavity shear layer as a portion of the fuel is convected into the cavity shear layer, mixed with the high-temperature gaseous products from the cavity, and ignited after some distance. Some high-temperature combustion products in the cavity shear layer are absorbed into the injection jet by the vortex interaction of the jet-with-cavity shear layer. Then, flame spreads gradually following the counter-rotating vortex induced by the jet until the whole injection jet is ignited. A portion of combustion products generated from the cavity shear layer and the jet is convected into the cavity interior by the unsteady motion of the cavity shear layer and transported with the recirculation flow to the cavity front wall. These hot products and their intermittent combustion then heat up the cavity and the fuel that enters into the cavity shear layer is preheated. Thus, the flameholding cycle is formed.

Acknowledgments

This work is supported by National Science Fund of China, grant number 90505009. Sincere thanks to Hou Zhongxi and Jin Liang of National University of Defense Technology for providing the fifth-order WENO scheme code and Menter's k–ω BSL model code.

References

[1] Gruber, M. R., Donbar, J. M., Carter, C. D., and Hsu, K-Y., "Mixing and Combustion Studies Using Cavity-Based Flameholders in a Supersonic Flow," *Journal of Propulsion and Power*, Vol. 20, No. 5, 2004, pp. 769–779. doi:10.2514/1.5360

[2] Ben-Yakar, A., "Experimental Investigation of Mixing and Ignition of Transverse Jets in Supersonic Crossflows," Ph.D. Thesis, Stanford Univ., Stanford, CA, 2000.

[3] Li, M. L., Zhou, J., Geng, H., and Zhai, Z., "Investigations on Function of Cavity in Supersonic Combustion Using OH PLIF," AIAA Paper 2004-3657, 2004.

[4] Choi, J-Y., Yang, V., Ma, F., Won, S-H., and Jeung, I-S., "DES Combustion Modeling of a Scramjet Combustor," AIAA Paper 2006-5097, 2006.

[5] Genin, F., and Menon, S., "LES of Supersonic Combustion of Hydrocarbon Spray in a SCRAMJET," AIAA Paper 2004-4132, 2004.

[6] Li, J., Ma, F., Yang, V., Lin, K-C., and Jackson, T. A., "Comprehensive Study of Combustion Oscillations in a Hydrocarbon-Fueled Scramjet Engine," AIAA Paper 2007-836, 2007.

[7] Ma, F. H., Li, J., and Yang, V., "Thermoacoustic Flow Instability in a Scramjet Combustor," AIAA Paper 2005-3824, 2005.

[8] Davis, D. L., and Bowersox, R. D. W., "Stirred Reactor Analysis of Cavity Flame Holders for Scramjets," AIAA Paper 97-3274, 1997.

[9] Baurle, R. A., Tarn, C.-J., and Dasgupta, S., "Analysis of Unsteady Cavity Flows for Scramjet Applications," AIAA Paper 2000-3617, 2000.

[10] Rasmussen, C. C., Driscol, J. F., Carter, C. D., and Hsu, K-Y., "Characteristics of Cavity-Stabilized Flames in a Supersonic Flow," *Journal of Propulsion and Power*, Vol. 21, No. 4, 2005, pp. 765–769. doi:10.2514/1.15095

[11] Rasmussen, C. C., Driscolla, J. F., and Hsub, K-Y., "Stability Limits of Cavity-Stabilized Flames in Supersonic Flow," *Proceedings of the Combustion Institute*, Vol. 30, No. 2, 2005, pp. 2825–2834. doi:10.1016/j.proci.2004.08.185

[12] Rasmussen, C. C., Dhanuka, S. K., and Driscoll, J. F., "Visualization of Flameholding Mechanisms in a Supersonic Combustor Using PLIF," *Proceedings of the Combustion Institute*, Vol. 31, No. 2, 2007, pp. 2505–2513. doi:10.1016/j.proci.2006.08.007

[13] Baurle, R. A., Tam, C. J., Edwards, J. R., and Hassan, H. A., "Hybrid Simulation Approach for Cavity Flows: Blending, Algorithm, and Boundary Treatment Issues," *AIAA Journal*, Vol. 41, No. 8, 2003, pp. 1463–1484.

[14] Spalart, P. R., Jou, W.-H., Strelets, M., Allmaras, S. R., "Comments on the Feasibility of LES for Wings and on a Hybrid RANS/LES Approach," *Proceedings of First AFOSR International Conference on DNS/LES*, Greyden Press, Columbus, OH, Aug. 1997, pp. 4–8.

[15] Menter, F. R., "Two Equation Eddy Viscosity Turbulence Models for Engineering Applications," *AIAA Journal*, Vol. 32, No. 8, 1994, pp. 1589–1605.

[16] Yoshizawa, A., and Horiuti, K., "Statistically Derived Subgrid Scale Kinetic Energy Model for Large-Eddy Simulation of Turbulent Flows," *Journal of the Physical Society of Japan*, Vol. 54, Aug. 1985, pp. 2834–2839.

[17] Fan, T. C., Xiao, X. D., Edwards, J. R., Hassan, H. A., and Baurle, R. A., "Hybrid LES/RANS Simulation of a Shock Wave/Boundary Layer Interaction," AIAA Paper 2002-0431, 2002.

[18] Xiao, X., Edwards, J. R., Hassan, H. A., and Baurle, R. A., "Inflow Boundary Conditions for Hybrid Large Eddy/Reynolds Averaged Navier–Stokes Simulations," *AIAA Journal*, Vol. 41, No. 8, 2003, pp. 1481–1489.

[19] Sun, M. B., Liang, J. H., and Wang, Z. G., "Improved Blending Function for Hybrid RANS/LES Methodology," *Proceedings of 2007 ISSP (International Symposium on Space Propulsion)*, Beijing University of Aeronautic and Astronautic Press, Beijing, 2007, pp. 503–517; also *Applied Mathematics and Mechanics* (submitted for publication).

[20] Yungster, S., Eberhardt, S., and Bruckner, A. P., "Numerical Simulation of Hypervelocity Projectiles in Detonable Gases," *AIAA Journal*, Vol. 29, No. 2, 1991, pp. 187–200.

[21] Mobus, M., Gerlinger, P., Bruggermann, D., "Scalar and Joint Scalar-Velocity-Frequency Monte Carlo PDF Simulation of Supersonic Combustion," *Combustion and Flame*, Vol. 132, No. 1, 2003, pp. 3–24. doi:10.1016/S0010-2180(02)00428-5

[22] Norris, J. W., and Edwards, J. R., "Large-Eddy Simulation of High-Speed Turbulent Diffusion Flames with Detailed Chemistry," AIAA Paper 97-0370, 1997.

[23] Sun, M. B., Liang, J. H., and Wang, Z. G., "Validation of an Uncoupled Solver of Non-Equilibrium Flow for Shock-Induced Combustion," *Journal of Aerospace Power* (to be published).

[24] Blin, L., Hadjadj, A., and Vervisch, L., "Large Eddy Simulations of Compressible Turbulent Flows," AIAA Paper 99-0787, 1999.

[25] Shu, C. W., "High Order ENO and WENO Schemes for Computational Fluid Dynamics," *High-Order Methods for Computational Physics*, edited by Barth, T. J., and Deconinck, H., Springer–Verlag, Berlin, 1999, pp. 439–582.

R. Bowersox
Associate Editor